INTERNATIONAL JOURNAL FOR NUMERICAL AND ANALYTICAL METHODS IN GEOMECHANICS
Int. J. Numer. Anal. Meth. Geomech., 2002; **26**:873–896 (DOI: 10.1002/nag.228)

Characterization and reconstruction of a rock fracture surface by geostatistics

A. Marache[1,2,*,†], J. Riss[1], S. Gentier[3] and J.-P. Chilès[3,‡]

[1] *CDGA—Université Bordeaux I. Av. des Facultés—33405 Talence Cedex, France*
[2] *Laboratoire MSS-Mat, UMR 8579—Ecole Centrale Paris, Grande Voie des Vignes—92295 Châtenay Malabry Cedex, France*
[3] *BRGM—3, Av. Claude Guillemin—BP 6009—45060 Orléans Cedex 2, France*

SUMMARY

It is well understood that, in studying the mechanical and hydromechanical behaviour of rock joints, their morphology must be taken into account. A geostatistical approach has been developed for characterizing the morphology of fracture surfaces at a decimetre scale. This allows the analysis of the spatial variability of elevations, and their first and second derivatives, with the intention of producing a model that gives a numerical three-dimensional (3D) representation of the lower and upper surfaces of the fracture. Two samples (I and II) located close together were cored across a natural fracture. The experimental data are the elevations recorded along profiles (using recording steps of 0.5 and 0.02 mm, respectively, for the samples I and II). The goal of this study is to model the surface topography of sample I, so getting estimates for elevations at each node of a square grid whose mesh size will be, for mechanical purposes, no larger than the recording step. Since the fracture surface within the sample core is not strictly horizontal, geostatistical methods are applied to residuals of elevations of sample I. Further, since structural information is necessary at very low scale, theoretical models of variograms of elevations, first and second derivatives are fitted using data of both that sample I and sample II. The geostatistical reconstructions are computed using kriging and conditional simulation methods. In order to validate these reconstructions, variograms and distributions of experimental data are compared with variograms and distributions of the fitted data. Copyright © 2002 John Wiley & Sons, Ltd.

KEY WORDS: rock joints; morphology; geostatistics; variogram; kriging; conditional simulation; fracture modelling; co-latitude; radius of curvature; hydromechanical behaviour

1. INTRODUCTION

Changes in stress and deformation in jointed rock masses are of prime importance in the assessment of stability in underground openings, in the optimization of petroleum and geothermal production, and in the design of dam foundations and waste storage facilities.

*Correspondence to: Antoine Marache, CDGA—Université Bordeaux I—Av. des Facultés—33405 Talence Cedex, France.
† E-mail: a.marache@cdga.u-bordeaux.fr
‡ Present address: Centre de Géostatistique—Ecole des Mines de Paris—35 Rue Saint-Honoré—77305 Fontainebleau, France.

Received 6 November 2001
Revised 20 March 2002

Therefore, it is necessary to understand the behaviour of jointed rock masses, and especially the mechanical and hydromechanical behaviour of individual fractures (under both normal and shear stresses). A necessary preliminary is thus an accurate knowledge of the morphology of fracture surfaces.

This morphology can be studied either by a global approach, by summarizing the deviation of the rough surface from an average plane by some morphological parameters [1,2], or by a full modelling of the detailed variations in the fracture surface. Since the hydromechanical behaviour of rock joints is governed by specific parts of the fracture surfaces, the second approach is one developed here. Geostatistical methods are used because they are designed to characterize spatial variations, and they provide consistent interpolation and simulations.

Profiles of elevations have been recorded on both walls of a granitic fracture (Guéret, France). The spatial relations between points of a surface (in terms of variation of elevations and their first and second derivatives) are characterized by means of geostatistical tools. Three-dimensional representations of the fracture surfaces are then built by geostatistical techniques (kriging, conditional simulations). Furthermore, to increase accuracy, the application shows how one might link data sets having very different sampling densities. Finally, the models are validated by comparing computed morphological parameters, chosen as important from a mechanical point of view, with experimental parameters.

2. PRESENTATION OF DATA

Fractures can be envisioned as two rough surfaces in partial contact. Each fracture surface has a complex geometry that determines its roughness. Since the two walls of the fracture are in partial contact, a void space exists between them (Figure 1). We study a natural fracture (Guéret granite, France). Two cylindrical samples were cored across this fracture. The fracture is located halfway up the cylindrical core sample and is approximately perpendicular to its axis (O_z). The first sample (I) is a cylindrical core with a diameter of 90 mm. Figure 2 shows a schema of the lower wall of the sample. Twenty-seven profiles of elevations (sampling interval $u = 0.5$ mm) have been recorded on the lower wall in four directions (a, b, c, d) allowing the creation of a database with 4096 co-ordinates $\{x, y, z\}$ [3] (Figure 3). In order to analyse the influence of its morphology during shearing [3], the choice of these four directions is linked to shear tests realized on replicas of the fracture. The spacing between two consecutive parallel profiles varies from 5 up to 15 mm. This spacing is not constant because profiles have been supplemented by others through damaged areas, located after shear tests. This data set can be considered representative. Similar profiles were recorded on the upper wall (4041 co-ordinates).

On the second sample (II) of the same fracture, profiles have been recorded along the radii of the cylindrical core with a sampling step of 0.02 mm. The two samples are separated by a few centimetres, and the axes of the two cylindrical cores are parallel to each other, since the fracture looks like a planar surface at the metre scale (that may no longer be true at a centimetre scale).

The aim of the study is to reconstruct the sample surface, more precisely to have a model for the elevations at the nodes of a fine grid on sample I using data of both samples (I and II); the size of the grid mesh will be either equal to or less than 0.5 mm (the recording step for sample I). We choose to reconstruct sample I because mechanical tests have been performed with replicas of this sample. Since the lower wall and the upper wall are very similar, we only present the analysis of the former. The tool used for the reconstructions is geostatistics because it allows the

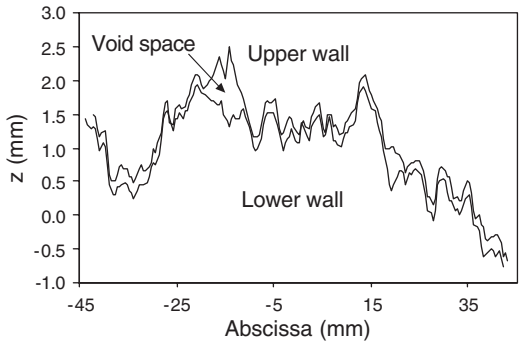

Figure 1. Example of two rough profiles and the resulting void space (note the different scale on the two axes).

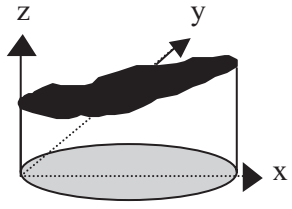

Figure 2. The lower wall of the fracture.

characterization of spatial relations between elevations, and enables the application of accurate mathematical methods of interpolation of experimental data.

3. GEOSTATISTICAL ANALYSIS OF RAW DATA

3.1. Variograms

The basic geostatistical tool for characterizing spatial variability is the variogram. It is experimentally computed as follows [4]:

$$\hat{\gamma}(h) = \frac{1}{2N_h} \sum_{x_j - x_i \approx h} [z(x_j) - z(x_i)]^2 \tag{1}$$

where z is the elevation, x_i is the location (in 2D), h is the lag vector, and N_h is the number of pairs of points, the distance apart from which is approximately equal to lag h.

Figure 4 shows directional variograms calculated with all sampled data for each of the four profile directions of sample I. The variogram stabilizes beyond 20 mm in direction b but increases with a quasi-parabolic behaviour in the other directions. This is typical of the presence of a trend, or drift, due to the fact that the mean plane of the fracture surface is not exactly orthogonal to the core axis.

Except for the b direction, we observe that $\gamma(h)$ fails to stabilize when h increases; its values are always increasing. This means that the phenomenon studied is not stationary. The mean value of the elevations is not constant in the directions a, c and d because the surface has a drift and is

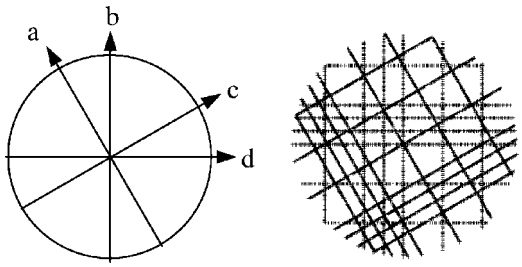

Figure 3. Location of the profiles on the lower wall.

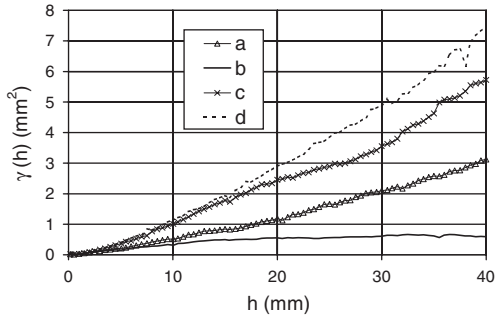

Figure 4. Directional variograms of elevation.

inclined at some degrees to the horizontal. This effect masks the spatial structure of elevation and thus has to be removed.

3.2. *Characterization of the drift*

Since elevations increase linearly on profiles in directions a, c and d, we consider the drift to be planar:

$$z_p(x, y) = ax + by + c \tag{2}$$

where x and y now explicitly denote the two co-ordinates perpendicular to the core axis.

This drift is usually approximated by the regression plane of the studied variable, z as a function of co-ordinates x and y. But since z is here a third co-ordinate, we did not want to assign a special role to z. So we chose to take the drift to be in the plane perpendicular to the third eigenvector of the covariance matrix of the initial set of co-ordinates [5,6]. This plane is inclined 5.03° to the horizontal, dipping with a direction of 178.16° measured anticlockwise from the x-axis. This is nearly parallel to the d direction. Figure 5 shows the relation between the measurement plane and this new plane using a stereographic projection.

We can now subtract the drift from the data and study the residuals.

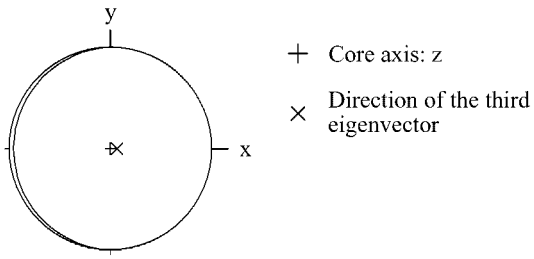

Figure 5. Relation between the core axis and the drift (Wulff projection of the lower hemisphere).

4. GEOSTATISTICAL ANALYSIS OF RESIDUALS

Residual values $z_r(x, y)$ are computed using Equation (3):

$$z_r(x, y) = z(x, y) - (ax + by + c) \tag{3}$$

where z is the experimental elevation at any point (x, y), and $(ax + by + c)$ is the drift value given by Equation (2).

Figure 6 shows an example of a profile in the d direction and the residual one: it is obvious on the residual profile that the drift has been removed.

The following geostatistical study is done on these residual values (variograms, reconstruction of the fracture surface).

4.1. Variograms

To compute variograms of data having drift, we can either use the generalized variogram [7], or compute variograms on the residual values (this latter is chosen here).

In the following, variograms are computed on residuals z_r. Furthermore, the distance u between two successive points along profiles being constant, the discrete first derivatives $z'_r(x, y)$ of residuals in each of the four directions and their variograms $\gamma_u(h)$ can also be computed. It should be noticed that for this the points must be strictly aligned. The expression of $z'_r(x, y)$ computed in the x direction is:

$$z'_r(x, y) = \frac{z_r(x + u, y) - z_r(x, y)}{u} \tag{4}$$

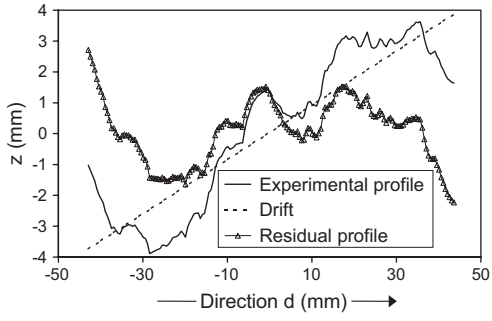

Figure 6. Experimental and residual profiles (note the different plotting scales on the two axes).

The use of variograms of first derivatives [8] is very efficient for fitting a theoretical model to variograms of experimental data. Since the discrete first derivatives are available, we propose the use of the variogram of the discrete second derivatives $\gamma_{u2}(h)$ as well.

The expression for the discrete second derivatives $z_r''(x, y)$ in the x direction is

$$z_r''(x, y) = \frac{z_r(x-u, y) - 2z_r(x, y) + z_r(x+u, y)}{u^2} \tag{5}$$

Figure 7 shows the three kinds of variograms: $\gamma(h)$, $\gamma_u(h)$, $\gamma_{u2}(h)$, obtained from the experimental data.

Analysis of variograms involves obtaining their structures. This means two values for each structure have to be determined. The first, the range, is the distance h beyond which values appear to be uncorrelated, and the second, the sill, is the value of $\gamma(h)$ at the range h.

With the calculus of variograms on residual values, the drift vanishes and the variograms of residuals reach a sill for each direction (between 0.6 and 1.2 mm^2, respectively, for the b and d directions). Differences between sill values show an anisotropy in the morphology of the residual fracture surface. The higher the sill is in a particular direction, the more the surface deviates from a planar surface. We observe the presence of a first structure at a range of 15 mm, then a second at a distance of 30 mm essentially in the c and d directions. This indicates that there exist at least two structures with different sizes characterizing the fracture surface. From a mechanical point of view, these structures do not have the same significance. The smaller

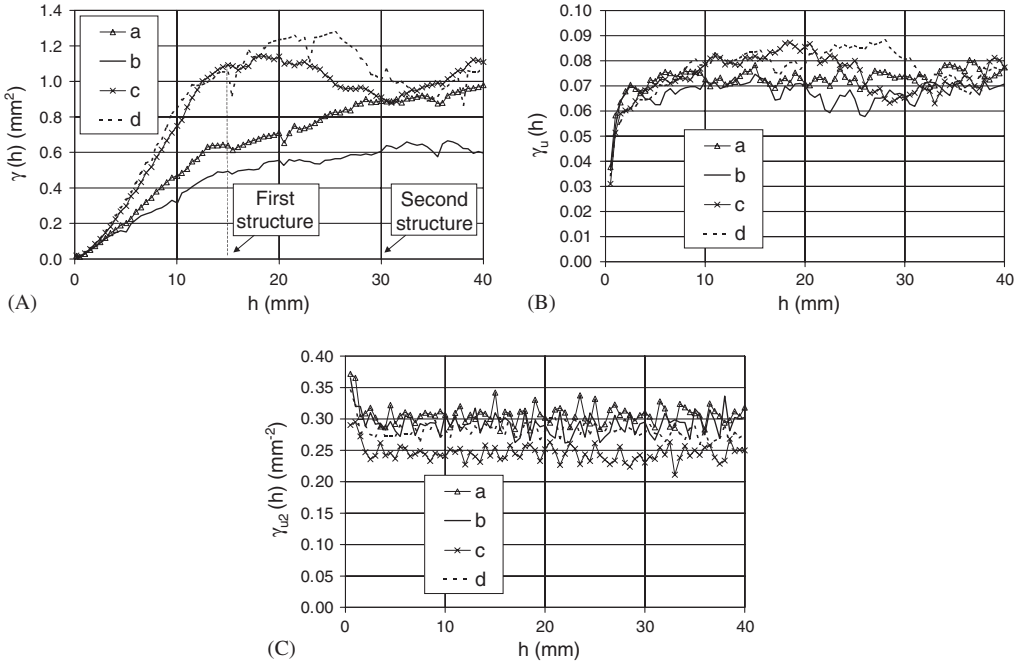

Figure 7. Experimental variograms of residuals (A), first derivatives (B) and second derivatives (C).

structure plays a role in shear behaviour for small displacements (local behaviour) and the greater for high displacements.

Opposed to variograms of residuals, anisotropy for the variograms of first and second derivatives is less obvious (Figure 7(B) and 7(C)). The higher the order of derivatives, the smaller the ranges of variograms of derivatives become (8 mm for the variograms of first derivatives, 2 mm for those of second derivatives), and the more the anisotropy decreases (the sills are very close to each other for the four variograms in both cases). First derivatives are linked to the angularity of an element of the fracture surface and second derivatives to the radius of curvature (cf. Section 5.2). These parameters seem to be less sensitive to the anisotropy of the fracture surface (this is most obvious with the second derivatives). Note that variograms of derivatives are exactly the same if they are computed on experimental values or on residual values because the drift is linear.

The aim is now to fit a first variogram model to the experimental one. This is a first variogram model because data of sample II are not being used yet. We will see later how to use this second data set to improve the variogram model.

4.2. *First variogram fitting*

In order to provide a 3D representation of the fracture surface we need to fit a theoretical model to experimental variograms. Furthermore to increase accuracy and to minimize errors in the reconstruction of fracture surfaces, we need the best fit not only for $\gamma(h)$ but for $\gamma_u(h)$ and $\gamma_{u2}(h)$ as well (u being the calculus step of derivatives).

The theoretical expressions of $\gamma_u(h)$ [8] and $\gamma_{u2}(h)$ as a function of $\gamma(h)$ are

$$\gamma_u(h) = \frac{2\gamma(u) + 2\gamma(h) - \gamma(h+u) - \gamma(h-u)}{u^2} \tag{6}$$

$$\gamma_{u2}(h) = \frac{8\gamma(u) + 6\gamma(h) - 2\gamma(0) - 2\gamma(2u) - 4\gamma(h+u) - 4\gamma(h-u) + \gamma(h+2u) + \gamma(h-2u)}{u^4} \tag{7}$$

A variogram model is defined as a sum of elementary models called nested models. The software we work with is Isatis [9]. Input parameters for computing a theoretical variogram must be the range and the sill (and sometimes a third parameter) of each of the nested models for the two main directions of anisotropy for the residuals. In order to find these two main directions of anisotropy, we compute the variogram map that represents the values of the variogram of residual values as a function of the distance h in all directions (Figure 8). Figure 8 shows the variogram map only up to a lag h equal to 10 mm. This is because it is sufficient to have a good fit between experimental and theoretical variograms up to an h of 8–10 mm since the estimation of a residual value will be performed with residuals of experimental points whose distance from the point to be estimated is less than or equal to 8–10 mm (see Section 4.5.2). The variogram map shows an elliptical shape whose main axes are the b and d directions. We therefore take the two main directions of anisotropy to be the b and d directions.

After a sequence of trials, the best model (called model 1) was the sum of four nested models (spherical, Cauchy and two cubic models, cf. Equation (8) and Table I). For this model, the sill is greater in the d direction than in the b one, according to experimental observations. Figure 9 shows the theoretical variograms and the experimental one for the two main directions. It can be seen that we have a good fit up to 8–10 mm for residuals, and a good fit with first and second

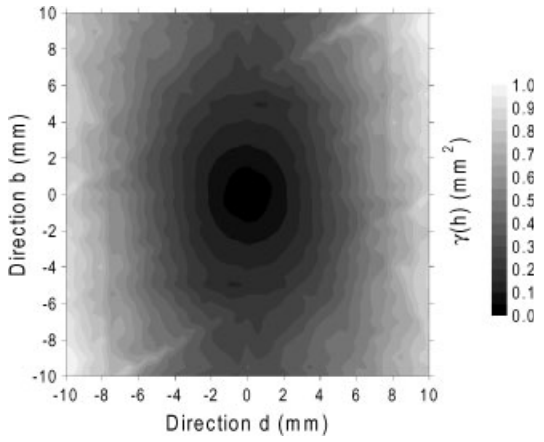

Figure 8. Variogram map of the residual values of the lower wall.

Table I. Fitted parameters for model 1.

Basic model	Sill (mm^2)	Range b (mm)	Range d (mm)	Other parameter
Spherical	0.09800	40.0	34	
Cauchy	0.06500	8.4	11	0.98
Cubic 1	0.70000	30.0	18	
Cubic 2	0.00105	0.9	1	

derivatives as well.

$$\textit{Spherical}: \quad \begin{cases} \gamma(h) = C\left(\frac{3}{2}\left(\frac{h}{a}\right) - \frac{1}{2}\left(\frac{h}{a}\right)^3\right) & \text{if } h < a \\ \gamma(h) = C & \text{if } h \geqslant a \end{cases}$$

$$\textit{Cauchy}: \quad \gamma(h) = C\left(1 - \frac{1}{(1+(\delta h/a)^2)^\alpha}\right) \qquad \begin{matrix} \alpha > 0 \\ \delta = \sqrt{20^{1/\alpha} - 1} \end{matrix} \tag{8}$$

$$\textit{Cubic}: \quad \begin{cases} \gamma(h) = C\left(7\left(\frac{h}{a}\right)^2 - 8.75\left(\frac{h}{a}\right)^3 + 3.5\left(\frac{h}{a}\right)^5 - 0.75\left(\frac{h}{a}\right)^7\right) & \text{if } h < a \\ \gamma(h) = C & \text{if } h \geqslant a \end{cases}$$

where C is the sill value, a is the range value, and h is the lag value.

Till now we have used only data of sample I. We want now to use data of the second sample (II) in order to improve the variogram model since the recording step is shorter than that for sample I. With the reduced recording step, improvement will arise out of microroughness.

4.3. Links with microroughness

Since the long-term goal is the understanding of the mechanical behaviour of rock joints, we need to estimate elevations of sample I at the nodes of a square grid with a mesh smaller than

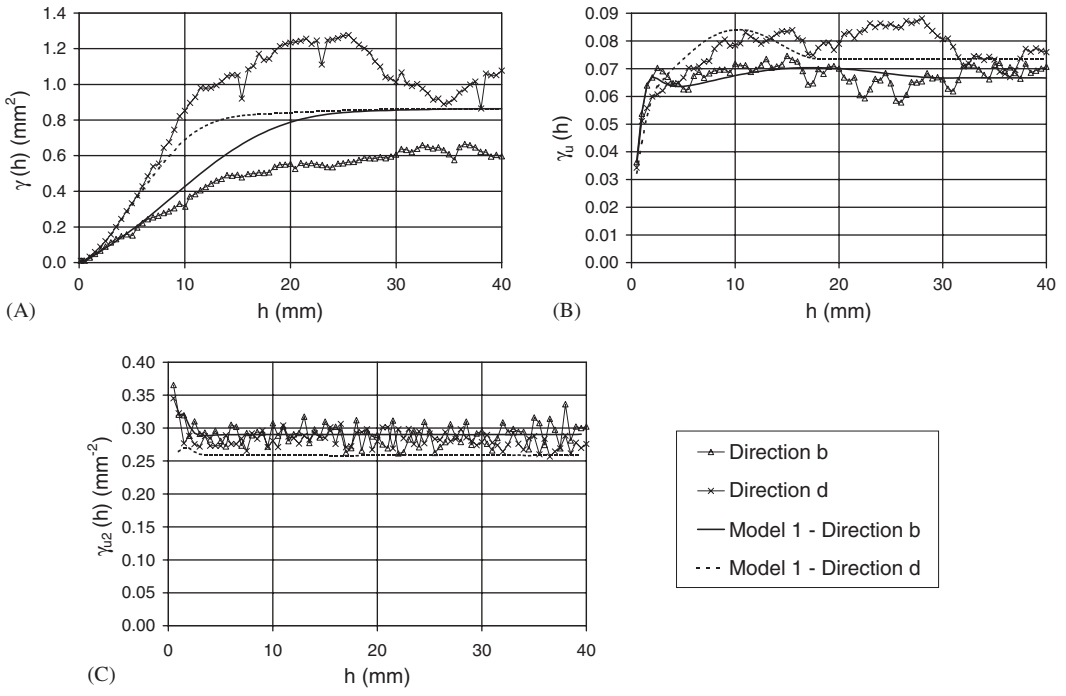

Figure 9. Variogram fitting to residuals (A), first derivatives (B) and second derivatives (C).

0.5 mm (the recording step of sample I). To improve the variogram model, we want to use measurements made on a second sample (denoted by II, having a diameter of 120 mm) located on the same fracture. On this sample, data are recorded every 0.02 mm, which enables the reconstructions with a grid mesh smaller than 0.5 mm. At this scale, variograms contain information about the texture of the rock (size of minerals for example) [10]. Since profiles are radii of the cylindrical sample, there are no preferential directions of recording. Furthermore, variograms of residuals computed on each profile separately are quite similar to one another. We therefore chose to compute an omnidirectional variogram of residuals, taking all directions into account, avoiding anisotropic considerations. First derivatives are computed in the same way as for sample I, but with a step of 0.02 mm. Then the final variogram of first derivatives is obtained by averaging all variograms computed on each profile separately (up to $h = 20$ mm). Note that the analysis of each variogram of first derivative separately (prior to averaging) shows a smaller anisotropy than for sample I. This is the reasoning behind working with a mean variogram.

Since we want to compare experimental variograms of sample II with model 1, we need for comparison to have only one variogram for model 1. Then we decide to average the two variograms of the main directions of anisotropy (b and d) (for residuals and first derivatives).

The comparison of variograms of residuals for samples I and II shows that variograms of sample II have higher values than those of sample I (Figure 10(A)). Since both data sets are comparable (samples located on the same fracture), we might have expected to get similar variograms, but it is not the case. Differences between variograms are due to either a greater variability of elevations of sample II or due to a support effect (measurements done on sample II

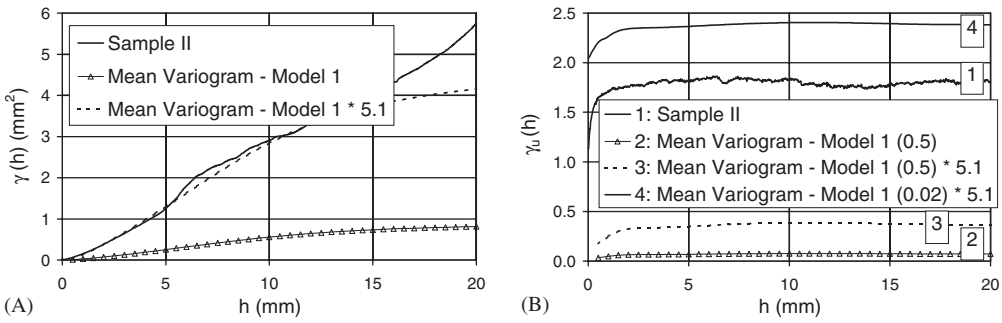

Figure 10. Variogram model of residuals (A) and first derivatives (B) for samples I and II (on B the number in parentheses indicates the step value u for the computation of derivatives).

being more accurate, we access details not available with the apparatus used on sample I). In order to improve the variogram model, we have to link these variograms. In order to take the observed greater variability of residuals of sample II into account, we propose adjusting the sill of model 1 to that of sample II (proportional effect). In order to do this we can multiply the values of model 1 by a constant factor, in this case, equal to 5.1. This constant is the ratio of the two sills (sample II and model 1). This is the technique usually adopted in geostatistics. Figure 10(A) shows that the variogram of sample II and modified model 1 are in good agreement.

The comparison of variograms of first derivatives also shows higher values for sample II (Figure 10(B), curves 1 and 2). If we multiply values of model 1 by 5.1, the constant factor, the sill of the resulting variogram remains lower than that of sample II (curve 3). In order to explain this, we can analyse more precisely the nested components of model 1. For a variogram of first derivatives, the smaller is the computation step of the discrete first derivatives, the greater is the sill of the variogram. As can be seen in Figure 11, values of the nested models decrease when the step u increases but not at the same rate, so they do not contribute equally to the final variogram. For computing Figure 11, the range and the sill are equal to 1, and the calculus of the variogram is done later than the range, so Equation (6) becomes

$$\gamma_u(h) = \frac{2\gamma(u)}{u^2} \quad \forall h \geqslant \text{range value} \tag{9}$$

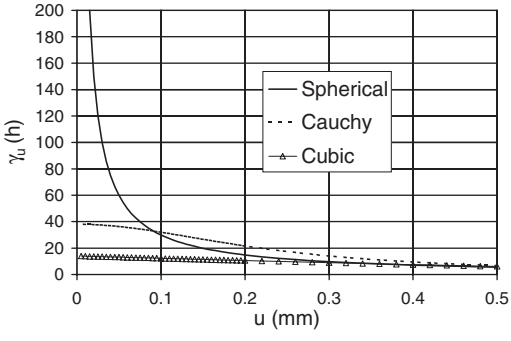

Figure 11. Influence of the step size u for first derivatives on the variogram.

Table II. Influence of the step u on the sill of model 1 and its components.

Nested model	$\gamma_u(h)$ (step 0.5 mm) A	$\gamma_u(h)$ (step 0.02 mm) B	Increase of sill B/A
Spherical	0.0159	0.3973	25.00
Cauchy	0.0260	0.0274	1.05
Cubic 1	0.0166	0.0170	1.02
Cubic 2	0.0067	0.0159	2.37
Model 1	*0.0652*	*0.4576*	*7.02*

We assume that this equation is available even for the Cauchy model. It should be noted that Figure 11 shows this phenomenon when h is greater than the range, but this remains true whatever the value of h.

As we know that the data set of sample I (and so of sample II too) is partially characterized by a spherical component, Figure 11 shows that the increase of $\gamma_u(h)$ values with the decrease of u is much greater for the spherical component than for the two others (Cauchy and cubic). In order to illustrate this proposition, we have used Equation (9) to compute $\gamma_u(h)$ values (Table II) for each component of model 1 (sills are those given Table I).

For a variogram having a linear behaviour at the origin (spherical variogram), the value of the sill is dependent on the step size u. This is not the case for variograms with a parabolic behaviour at the origin (Cauchy, cubic). That is why for the spherical component, the sill is multiplied by 25 when size step u is divided by 25. The presence of the others components reduce the influence of the spherical model, so the increase of sill is equal to a factor 7 when u changes from 0.5 to 0.02 mm. The sill of model 1 is theoretically multiplied by about $7 \times 5.1 = 35.7$ (where 5.1 was due to the greater variability of data of sample II). As a consequence the resulting variogram (Figure 10(B), curve 4) shows higher values than those of the experimental one (curve 1). It will be shown how to take these observations into account in order to improve the model.

4.4. *Final variogram model*

To search the final variogram model, we start from model 1 and we modify it according to the previous considerations. We would like a fit of this new model to variograms of residuals and first derivatives of samples I and II and to variograms of second derivatives of sample I (Figure 12). The final model, called model 2, is the sum of five nested models (spherical, two Cauchy and two cubic models, Table III). The model is well fitted to experimental variograms up to a lag h of 8–10 mm.

In conclusion, it can be seen that the improvement to the fit is not entirely obvious from Figure 12(A)–12(D), but is clearly seen in Figure 12(E) (the variogram of first derivatives of sample II is very close to that of model 2).

The next step is to use the variogram model 2 so as to reconstruct sample I, and obtain an elevation at each node of a square grid covering the sampled surface.

4.5. *Reconstruction of the fracture surface*

The reconstruction of fracture surfaces consists of an interpolation based on the theoretical variogram model and on experimental data in order to estimate the elevation at each node of a given grid. Two methods are commonly used: kriging and conditional simulation [11].

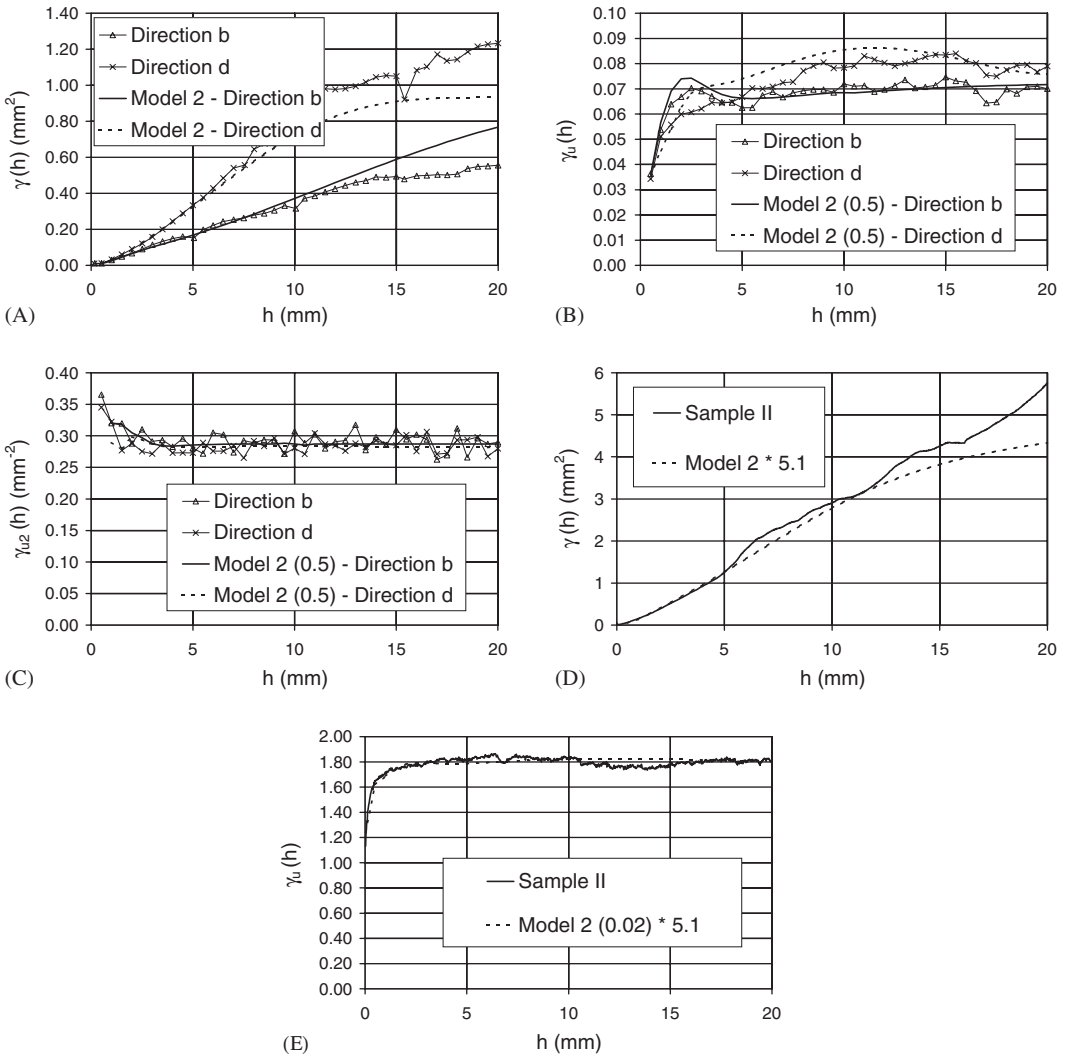

Figure 12. Final variogram fitting to residuals (A), first derivatives (B) and second derivatives (C) of sample I and to residuals (D) and first derivatives (E) of sample II.

Table III. Parameters of model 2.

Basic model	Sill (mm^2)	Range *b* (mm)	Range *d* (mm)	Other parameter
Spherical	0.025	10.0	40.0	
Cauchy 1	0.062	4.0	4.8	4.00
Cauchy 2	0.001	200.0	300.0	0.19
Cubic 1	0.850	38.0	20.0	
Cubic 2	0.003	1.8	1.1	

4.5.1. Kriging and conditional simulation. Kriging is a method of unbiased estimation based on a linear interpolation that minimizes the variance of estimation. A consequence is that it smoothes local fluctuations.

Let x be the value to be estimated, n the number of points used for the estimation, and γ the value of the variogram model. The objective of kriging is the solution of the following linear system of equations ($n+1$ equations for $n+1$ unknown variables).

For $i = 1, 2, \ldots, n$:

$$\sum_{j=1}^{n} \lambda_j \gamma(x_i - x_j) + \mu = \gamma(x_i - x)$$

$$\sum_{j=1}^{n} \lambda_j = 1 \tag{10}$$

This system minimizes the variance of unbiased estimation.

The parameter n is defined either as the total number of experimental data if we work within a global neighbourhood when n is not too large, or as a sufficiently large number of points (usually between 15 and 20) chosen with an homogeneous spatial distribution in the neighbourhood of the point to be estimated (moving neighbourhood).

In Equation (10), the unknown variables are:

- λ: the weights attached to the points used for estimation as a function of the distance from the point used for the estimation and its true value. These weights are the solutions of the kriging system and are a function of the distance between points used for the estimation (the consequence of the solution is to avoid the influence of large densities of points).
- μ: Lagrange's multiplier.

The variance of estimation or kriging variance can be defined as follows:

$$\sigma_K^2 = -\gamma(0) + \mu + \sum_{j=1}^{n} \lambda_j \gamma(x_j - x) \tag{11}$$

The weakness of kriging is its tendency to smooth. In order to introduce variability into the result, another method of interpolation is used, that of conditional simulation. If kriging is a method of estimation, conditional simulation is a method of simulation.

The conditional simulation technique allows the introduction of variability based on experimental data, so local fluctuations are not smoothed. Conditional simulation is a combination of a non-conditional simulation and a kriging. A non-conditional simulation simulates a field of values having the same spatial structure as the initial field of data. Combined with kriging, conditional simulation is conditioned by experimental data, so the best estimation of an experimental data is its measured value (as for kriging). The main methods of conditional simulation (turning bands, sequential Gaussian simulation) require that the initial data set has a Gaussian distribution. If not, a transformation to Gaussianity is necessary. Conditional simulation allows the introduction of variability, but the variance of the simulation is twice that of kriging.

4.5.2. Application to rock fracture surfaces. Various reconstructions based on residuals of elevations of sample I have been computed. Since the drift had been removed (cf. Section 4), it

will have to be restored at the end of the reconstruction in order to get elevation values comparable with those of recorded profiles. These reconstructions have been computed either by kriging or conditional simulation, but also by a combination of the two methods. Kriging is preferred if we want to minimize errors during reconstruction, but it smoothes estimated values. If we want to introduce variability and local fluctuations, conditional simulation is better. This latter technique is efficient for the knowledge of elevations between experimental profiles (areas with a lack of experimental data) and for reconstructions realized with a step less than 0.5 mm. In fact, for mechanical reasons, we want to obtain reconstructions with a small step in order to study micromechanisms of deformation.

To perform reconstructions, the following method has been developed.

Reconstructions are performed in several stages from a coarse to a fine grid. For each stage, to estimate the residual value at a given point, we work with data located in a neighbourhood circle of radius 8 or 10 mm (according to the variogram model) around the point to be estimated (that is why the best fit was sought at the beginning of the variogram, cf. Sections 4.2 and 4.4). This circle is divided into height sectors and the number of points taken is the same in each sector (with an optimum choice of 10 per sector).

Furthermore, the variogram model having been fitted for $h = 0.02$ mm, we can realize reconstructions of sample I with a step shorter than 0.5 mm. We choose to perform reconstructions with a square mesh of 0.1 mm. This size is sufficient also for the study of shearing for small horizontal displacements and hydraulic behaviour.

Various kinds of reconstructions of sample I are realized depending on the choice of the grid mesh size, the minimum distance between points used for the estimation, and the geostatistical method (kriging or conditional simulation for each step). For conditional simulation, various kinds of numerical methods are used: turning bands or sequential Gaussian simulation [11]. Recall that for the use of conditional simulation, we must have a Gaussian distribution of residuals (necessary but not sufficient in theory) (cf. Section 4.5.1). Chi-square tests of fit have been carried out comparing the experimental distributions of residuals with a Gaussian distribution (having the same mean value and same standard deviation). Results of the tests are good for all classical confidence levels (90%, 95% and 99%). Furthermore we choose other different parameters: the number of simulations averaged for the final result (because one simulation gives too big a variability in the reconstruction), and the size of the neighbourhood. The optimal number of simulations averaged is found after several trials. After each attempt a validation of the reconstruction is done (cf. Section 5) and the number of averaged simulations is modified or not, depending on the results of the validation.

The first stage is always a reconstruction on a 2 mm grid mesh with a minimum distance of 1.5 mm between estimation points. This is to avoid the experimental points being too close to one another. After each step and before computing the next using a finer grid, points resulting from the reconstruction are added to the experimental ones in order to get a more homogeneous spatial distribution of data. This technique in several stages is based on the three perpendiculars theorem [11].

The proposed method shows how to link two data sets and how to get various reconstructions from a coarse to a fine grid.

Figure 13 shows results of a geostatistical reconstruction performed by kriging for sample I. To improve the images, the fracture surfaces in Figure 13 are shown with a mesh bigger than 0.5 mm, although this reconstruction is the result of a first kriging with a minimum distance

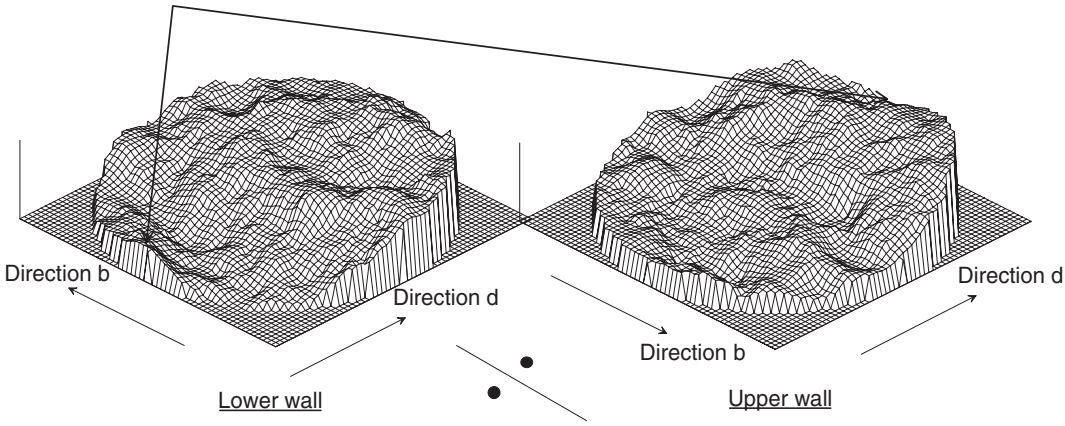

Figure 13. Lower and upper walls of sample I reconstructed by kriging.

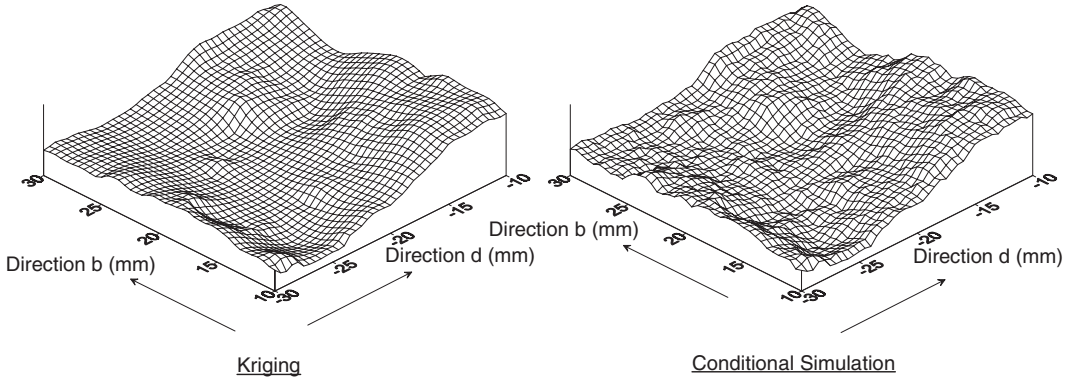

Figure 14. Part of the lower wall reconstructed by kriging and by conditional simulation.

between experimental points used of 1.5 mm on the 2 mm grid followed by a second kriging with a grid mesh of 0.5 mm.

Figure 14 shows a part of the lower wall in order to appreciate differences between the two main methods of reconstruction. The two methods used for comparison are the reconstruction done by the previous described kriging and a reconstruction done by a conditional simulation realized by turning bands (average of five simulations after the first step and of six simulations after the second one). The grid mesh in Figure 14 is here equal to 0.5 mm.

One can see on Figure 14 that the fracture surface reconstructed by kriging seems smoother than that reconstructed by conditional simulation. The smoothing due to the kriging method is expected theoretically.

We have seen that when we use conditional simulation, we need to average n simulations in order to get a variability matching the experimental one. But in theory, a single simulation is sufficient to obtain representative variability. It is interesting to study why this should be.

4.5.3. The method developed and conditional simulation. We have seen that we need to average n conditional simulations in order to get the experimental variability after reconstruction. This is

obvious when we compute variograms of first and second derivatives after reconstruction. This proves that there is redundancy somewhere in our reconstruction method. In fact, there is certainly a very small nugget effect that is not accounted for in the variogram model. A nugget effect offsets the variogram at the origin. In such a study, a nugget effect can be linked to the measurement error. Furthermore, even if we introduce a nugget effect into the variogram model, we would still have a problem with the variability after conditional simulation because the nugget effect is not simulated by the methods of conditional simulation. This fact is emphasized when we calculate the first or second derivatives.

We conclude that taking the average of n simulations to get the experimental variability can be a good solution to filter out deficiencies in the method of reconstruction.

We have to now validate the reconstructions with objective criteria.

5. VALIDATION OF RECONSTRUCTIONS

The aim of this section is to validate the reconstructions by comparing experimental variograms or distributions of morphological parameters (co-latitudes in two dimensions and radii of curvature) with those computed from reconstructions. The quality of a reconstruction depends of the agreement between experimental and inferred data.

Results presented in this section are derived from various reconstructions of the lower wall of sample I (grid mesh 0.5 mm). The two methods of reconstruction used for comparison are the same than those used for Figure 14. We choose these two reconstructions because their results are well representative of all the others; furthermore, we have experimental variograms and morphological parameters only for a step of 0.5 mm. If we want to validate reconstructions realized with the 0.1 mm grid mesh, we could compare only variograms computed on reconstructions with the variogram model.

5.1. Variograms after reconstruction

In order to validate the reconstructions, we compute variograms of residuals, first and second derivatives with the complete set of data points resulting from reconstructions. Figure 15 shows the different variograms computed for both the reconstructions previously described and the experimental variograms in the b and d directions.

One can see that variograms computed on residuals resulting from reconstructions are quite close to one another (Figure 15(A), curves 3, 5 and 4, 6) and are in good agreement with the experimental variograms (Figure 15(A), curves 1 and 2), except for great values of h in the d direction.

The main difference between the methods is seen on the variograms of first and second derivatives. For kriging (Figure 15(B) and 15(C), curves 3 and 4), these variograms have lower sills than the experimental one (with underestimation of 50% on the sill of the variograms of first derivatives and of 80% on those of second derivatives). This result could have been deduced theoretically. Since the fracture surface is smoothed, consequences of this smoothing appear stronger when we compute derivatives of residuals, underestimating the sill of the variograms. For conditional simulation, the sill observed on variograms of derivatives depends on the number of simulations used for averaging. One can see that with conditional simulation, the variograms of the first derivatives are of good quality, but the variograms of the second

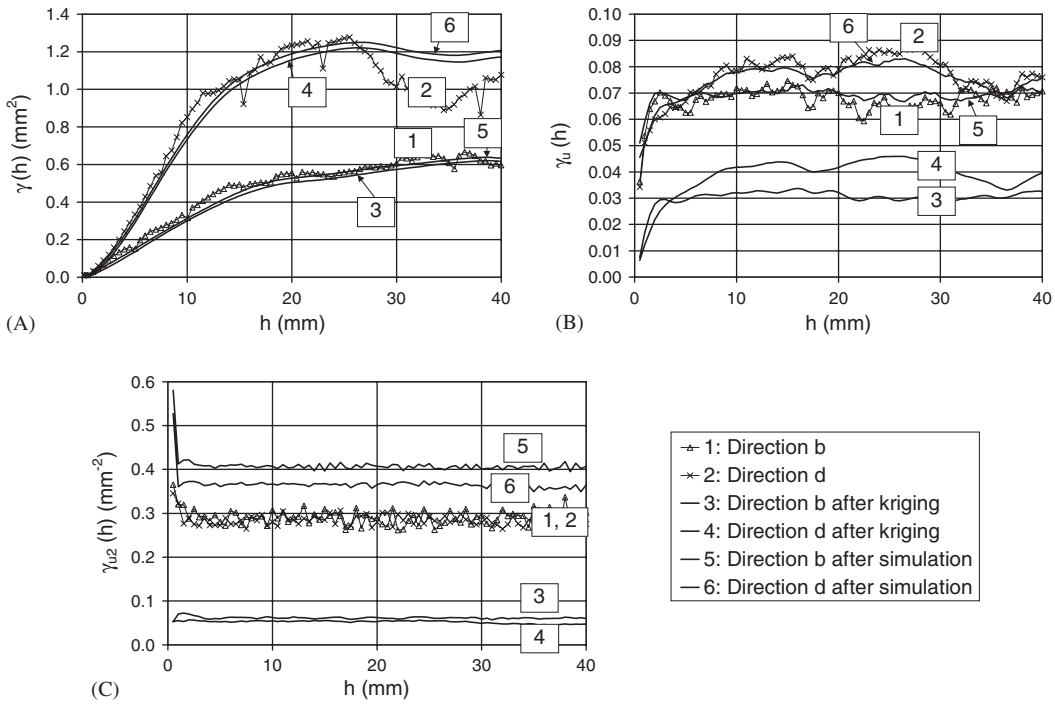

Figure 15. Variograms of residuals (A), first derivatives (B) and second derivatives (C) computed on experimental and interpolated data.

derivatives show sill values that are too high (overestimation of 31%). This observation could be a defect in our reconstruction (an overestimation of the variance of second derivatives), but it is very small compared with the improvement of the model due to the use of second derivatives.

In conclusion, it should be emphasized that the use of variograms is very efficient since, first, it permits the realization of reconstructions and, secondly, it allows also identification of the better reconstructions in regard to our mechanical needs. For example, if we want to study micromechanisms of deformation, conditional simulation will be preferred because the variability is greater for short distances between points than with kriging. This has also implications to study fluid flow in the fracture because the distribution of voids and their connection depend on the results of the reconstructions. But if we study the mechanical behaviour on the centimetre or decimetre scale, results of kriging and conditional simulation are very close. The reconstructions used depend on what is needed, and particularly on the scale of study.

5.2. *Calculus of morphological parameters*

In rock mechanics it is common to compute distributions of variables such as co-latitudes or radii of curvature in order to characterize the morphology of fracture surfaces [1]. We decided, therefore, to compare the distributions of these variables for experimental and interpolated data. These computations are realized on elevations: residuals plus the value of the drift for each

point. The following comparison is done between experimental distributions and those obtained after a conditional simulation (again, distributions after kriging show the smoothing effect).

5.2.1. Calculus of co-latitudes in two dimensions. In two dimensions, the co-latitude of a segment is the angle made by its normal and a reference axis. Here the reference direction is the z-axis. In a given direction (x for example):

$$\theta_2(x, y) = \arctan\left(\frac{z(x+u, y) - z(x, y)}{u}\right) \tag{12}$$

Distributions of co-latitudes (θ_2) can be computed for each direction, either on experimental data or on results of geostatistical reconstructions with a step u equal to the grid mesh. Positive and negative values are taken into account (Figure 16).

Figure 17 shows cumulative frequencies of co-latitudes computed for experimental data for each direction.

By looking at the median values in Figure 17, one can see that the c and d directions have the greatest proportion of positive values and the a direction has the greatest proportion of negative values (c and d directions are close to the direction of dip of the planar drift).

Figure 18 shows cumulative frequencies of co-latitudes computed with inferred data for the d direction and for kriging and conditional simulation.

With conditional simulation (Figure 18), the distribution is very close to that from experimental data (confirmed by the chi-square tests). This shows that we cannot reject the hypothesis of similarity between the experimental and conditional simulation distributions for

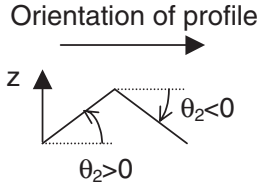

Figure 16. Definition of a co-latitude in two dimensions.

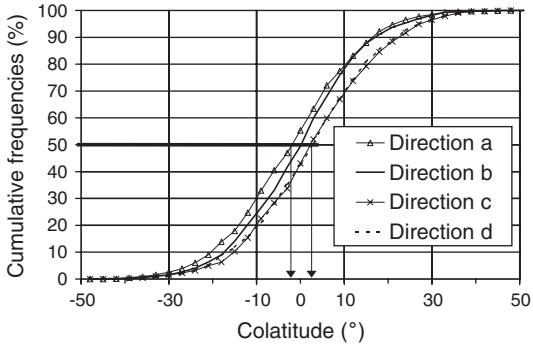

Figure 17. Experimental distributions of co-latitudes (distributions are very closed for the c and d directions).

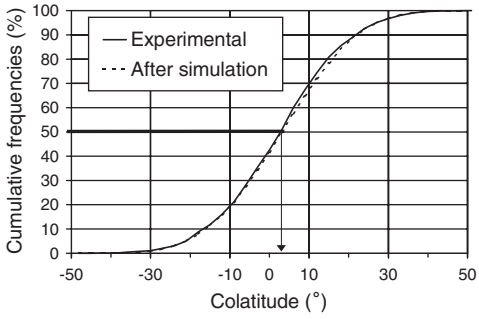

Figure 18. Distributions of co-latitudes in the d direction after simulation.

the classical confidence levels (90%, 95% and 99%). These observations hold also for the results from the other directions. Note also that the median simulated value is the same as the experimental one.

In order to characterize the distributions, we can compute statistical parameters. We choose here to compute the mean value of each distribution. The mean value of n angular values is computed as follows [12]:

$$\bar{\theta} = \arctan\left(\frac{\sum_{i=1}^{n} \sin(\theta_i)}{\sum_{i=1}^{n} \cos(\theta_i)}\right) \tag{13}$$

Table IV gives mean values for positive and negative co-latitudes for each direction and the associated percentage of pairs of points used for the calculus.

The closer the direction of calculation to d (the direction of dip of the drift) the more we have positive co-latitudes, in both percentage and value terms.

Lastly, the knowledge of co-latitudes in two dimensions is very important because we know that this morphological parameter has a primordial role in the shear behaviour of rock joints [13].

5.2.2. Radii of curvature. Assuming that profiles of elevations are curves, we can compute their radii of curvature. To compute the radius of curvature we calculate a polynomial approximation of order 2 (Figure 19) for a subset of k consecutive points along the profile. Since we need to analyse the fracture in detail, we choose $k = 3$ because it is known that, for planar surfaces, the smaller the number of points k that is used the smaller is the value of the radius of curvature, so

Table IV. Co-latitude mean values.

	$\theta_2 \geqslant 0$ (°)	Percentage of pair of points (%)	$\theta_2 \leqslant = 0$ (°)	Percentage of pair of points (%)
Experimental b	10.47	50.60	− 11.32	49.40
Experimental d	12.55	57.43	− 10.96	42.57
Simulation b	11.37	49.03	− 11.44	50.97
Simulation d	12.97	58.36	− 10.79	41.64

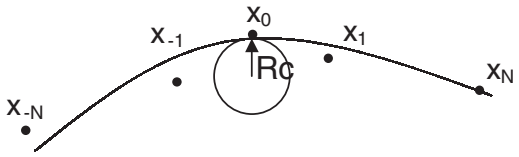

Figure 19. Definition of an element for the radius of curvature calculus.

Table V. Definition of each element as a function of first and second derivatives.

First derivative	>0	>0	<0	<0
Second derivative	>0	<0	>0	<0
Name	P–P	P–N	N–P	N–N
Significance				

the distribution of radii of curvature has a greater variability. We demonstrate the radius of curvature value at the point x_0, as shown in Figure 19.

The radius of curvature is computed as follows in the x direction:

$$R_c = \frac{(1 + (\partial z/\partial x)^2)^{3/2}}{|\partial^2 z/\partial x^2|} \tag{14}$$

where z is the approximated value computed in the x direction.

With the knowledge at each point of the first and second derivatives (concavity), we can combine it with the radii of curvature to define four types of element (Table V).

Any positive first derivative corresponds to a positive co-latitude as defined in the previous section.

Figure 20 shows cumulative frequencies of radii of curvature, in respect of the classification defined in Table V, computed on experimental data for the b and d directions.

Comparing Figure 20(A) and 20(B), one can see that experimental distributions of radii of curvature are nearly identical in all directions. Nevertheless, small differences appear,

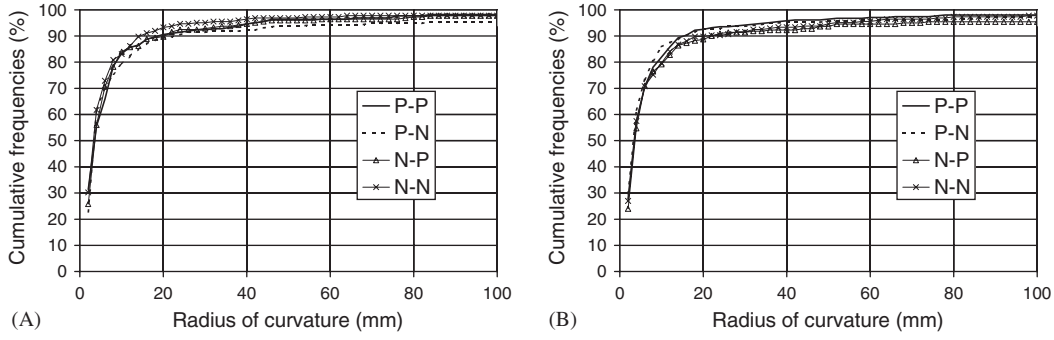

Figure 20. Distributions of experimental radii of curvature for the b (A) and d (B) directions.

principally up to a value of radius of curvature equal to 20 mm. In the *d* direction, there are more small values of radii of curvature for the P–P and P–N kinds (with fewer for the two other kinds) than for the *b* one. Furthermore, in each direction, the four curves plotted for each kind of element are close one to each other, but the same little differences appear. Since radii of curvatures are linked to second derivatives, this confirms the note made on variograms that the higher the order of derivative the more the anisotropy disappears.

Figure 21 shows cumulative frequencies of radii of curvature (P–P and P–N kinds) calculated on inferred data for the *d* direction and for conditional simulation. Only the P–P and P–N kinds of radius of curvature are presented in this paper, but the conclusions hold for all kinds of radius of curvature.

Conditional simulation shows that there are slightly more low values than for the experimental distributions (see for example the 80% decile on Figure 21(A)). This conclusion confirms the observation made regarding variograms of second derivatives (Figure 15(C)) that reconstructions realized with conditional simulation overestimate second derivatives, so small values of radii of curvature as well.

In order to characterize the distributions, we choose to calculate medians because means are strongly influenced by the highest values. Table VI gives medians for P–P and P–N types and the percentage of triplet of associated points.

One can see that the percentage of points is more important when the direction used in the calculation is close to the drift dip (as for the co-latitudes) and that the percentage of triplet of points is about the same for both P–P type and P–N type. For simulations, the observed median values confirm that there is an overestimation of low radii of curvature.

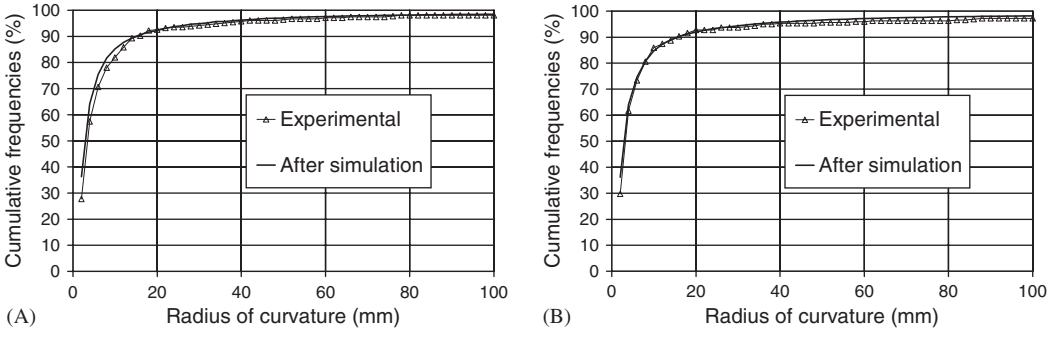

Figure 21. Distributions of radii of curvature for the *d* direction for P–P (A) and P–N (B) kinds.

Table VI. Characterization of P–P and P–N radii of curvature.

	$P–P_{50}$ (mm)	Percentage of triplet of points (%)	$P–N_{50}$ (mm)	Percentage of triplet of points (%)
Experimental *b*	3.27	24.64	3.11	25.64
Experimental *d*	3.31	28.81	3.22	29.65
Simulation *b*	2.44	24.33	2.54	24.67
Simulation *d*	2.74	29.95	2.73	30.07

Table VII. Characterization of P–N radius of curvature with different deciles or quartiles.

	Q10 (mm)	Q25 (mm)	Q50 (mm)	Q75 (mm)	Q90 (mm)
Experimental *b*	1.29	2.03	3.11	7.76	22.96
Experimental *d*	1.34	1.84	3.22	6.62	15.73
Simulation *b*	1.00	1.45	2.54	5.51	13.91
Simulation *d*	1.09	1.58	2.73	6.12	15.46

In order to characterize more accurately the radii of curvature distributions, we can compute other deciles and quartiles (10%, 25%, 75% and 90%). Table VII gives these different deciles or quartiles for the P–N kind of radius of curvature and for the experimental distributions and after conditional simulation distributions.

For the experimental distributions of radii of curvature, one can see that the main difference between directions *b* and *d* is marked with the Q90 decile. In fact, there are more high values of radii of curvature for the *b* direction than for the *d* one. This is again due to the direction of dip of the drift. When this direction is close to that of the drift (*d*), the proportion of small values of radii of curvature is greater because of the greater roughness.

Results of conditional simulation show a good agreement with experimental results. The agreement is better for the *d* direction than for the *b* one, principally for the Q75 and Q90 values. This observation could be deduced from the analyses of the variograms of second derivatives after reconstruction (Figure 15(C)). On this graph, for conditional simulation, the curve of the *d* direction is closer to the experimental variogram than for the *b* direction, so it is obvious that results of radii of curvature are in better agreement with the *d* direction.

In conclusion, it is very interesting to observe that the qualitative analysis of the results of the previous morphological parameters could be done entirely by analysis of the variograms, confirming their power as a geostatistical tool.

Till now, geostatistics has been used to analyse fracture surfaces without mechanical considerations. In the next section, an example of the use of geostatistics linked to rock joint mechanical behaviour is presented.

6. EVOLUTION OF VARIOGRAMS WITH THE SHEAR PROCESS

The calculus of directional variograms can also be used to analyse the evolution of the roughness during a shear test on rock joint [14]. In order to study this evolution, mortar replica of the granitic joint have been made and shear tests have been realized by keeping always the same morphology of rock joint surfaces. These tests have been realized in various directions, under various levels of normal stress. Furthermore the tests have been stopped at various level of horizontal displacements in order to record the same profiles of elevations than on the intact walls. On a same profile, variograms can be computed for different horizontal displacements. Variograms of elevations presented in Figure 22 have been calculated on one profile after a shear test in the *b* direction under a constant normal stress equal to 21 MPa.

One can see in Figure 22 that variograms are different as a function of the horizontal displacement because there is an evolution of the morphology, creation of damaged areas on fracture surfaces, with the shear process. When the horizontal displacement increases,

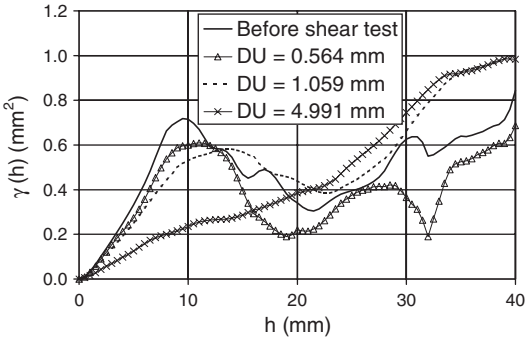

Figure 22. Variograms of elevation before and after a shear test.

Table VIII. Evolution of variogram parameters with the horizontal displacement.

ΔU (mm)	Slope at the origin (mm)	Range (mm)	Sill (mm^2)
0.000	0.067	9.5	0.72
0.564	0.055	11.0	0.61
1.059	0.051	13.5	0.58
4.991	0.025	—	—

consequences on variograms are a decrease of the slope at the origin and of the sill, and an increase of the range. This is because after the shear process the joint surface is smoother than before the shear process. These parameters are summarized in Table VIII. But on this example, for the greater horizontal displacement, sill and range disappear. This is the consequence of a big change in the morphology and the creation of a drift in the topography in this direction. This drift is certainly due to the distribution of gouge material on the profile.

One of the future developments could be to find a relation to predict the evolution of the variograms as a function of the horizontal displacement.

7. CONCLUSION

In a lot of domains, like stability of rock masses or waste storage, an accurate knowledge of the behaviour of jointed rock masses is needed. In order to understand the hydromechanical behaviour of jointed rock masses, it is necessary to study the hydromechanical behaviour of isolated rock joints under normal and shear loads. It is today well accepted that this behaviour is closely linked to the morphology, to the roughness of fracture surfaces. So the first step is to obtain a good numerical model of the fracture surface for use later in mechanical and hydraulic computer calculus [15].

To characterize the morphology of the joint in terms of spatial variability between data points and to reconstruct it, the geostatistical tool allows us to obtain sufficient and accurate knowledge of the morphology. The proposed method of characterization and reconstruction is to study the elevations and their residuals (eliminating any drift), first and second derivatives,

and take the anisotropy of the data into account. It shows how to link two data sets in order to improve the quality of the reconstruction. The example of a granitic fracture demonstrates the power of this method in that it gives different reconstructions, from a coarse to a fine grid, with different geostatistical methods. The reconstructions are validated and the computed parameters in the validation are in good agreement with experimental data. With this work, we know exactly the best reconstruction as a function of what is needed for future mechanical studies. Furthermore, it is important to note that the analysis of variograms on its own gives a lot of information, even on morphological parameters classically computed by rock mechanics.

We have shown the power of the geostatistical tool for the characterization and the reconstruction of rock fracture surfaces. Furthermore, this tool can be used in many others applications: characterize more accurately the void space [16] or find structural links between fracture surface heights and void space before or after shearing [17].

This geostatistical study is only a first step, but an essential step, towards improving hydromechanical behaviour models of rock joints. Further, the proposed method can be applied to all kinds of rock fractures.

ACKNOWLEDGEMENT

The authors would like to thank R. Coleman for his comments on this paper.

REFERENCES

1. Gentier S. Morphologie et comportement hydromécanique d'une fracture naturelle dans le granite sous contrainte normale—Etude expérimentale et théorique. *Thèse* de l'Université d'Orléans—Speciality Rock Mechanics, 1986.
2. Sabbadini S, Homand-Etienne F, Belem T. Fractal and geostatistical analysis of rock joint roughness before and after shear tests. *Proceedings of the 2nd Mechanics of Jointed and Faulted Rocks*. Vienna, 10–14 April, 1995; 535–541.
3. Flamand R. Validation d'une loi de comportement mécanique pour les fractures rocheuses en cisaillement. *Ph.D.* of the University of Quebec at Chicoutimi—Speciality Mineral Resources, 2000.
4. Armstrong M. *Basic Linear Geostatistics*. Springer, Berlin, 1998.
5. Riss J, Gentier S, Archambault G, Flamand R, Sirieix C. Irregular joint shear behaviour on the basis of 3D modelling of their morphology: morphology description and 3D modelling. *Proceedings of the 2nd Mechanics of Jointed and Faulted Rocks*. Vienna, 10–14 April, 1995; 157–162.
6. Marache A, Riss J, Lopez P, Gentier S. Geostatistical modelling of a fracture surface: implication in shear simulation by image analysis. *STERMAT 2000*, Krakow, September 20–23, 2000; 265–271.
7. Chilès J-P. Le variogramme généralisé. *Rapport N*-612, Fontainebleau, 1979.
8. Chilès J-P, Gentier S. Geostatistical modelling of a single fracture. *Geostatistics Troia' 92*, *International Congress for Geostatistics*, **vol. 1**, 1992; 95–108.
9. Isatis. Geovariances; Release 3.1.5 (1998).
10. Wu J. Description quantitative et modélisation de la texture d'un granite: granite de Guéret. *Thèse* de l'Université Bordeaux I, France, Speciality Applied Geology, 1995.
11. Chilès J-P, Delfiner P. *Geostatistics—Modeling Spatial Uncertainty*. Wiley-Interscience: New York, 1999.
12. Mardia KV. *Statistics of Directional Data*. Academic Press: New York, 1972.
13. Lopez P, Riss J, Gentier S, Flamand R, Archambault G, Bouvet S. Image analysis and geostatistics for modeling shear behavior. *Image Analysis and Stereology* 2000; **19**(1):61–65.
14. Roko RO, Daemen JJK, Myers DE. Variogram characterization of joint surface morphology and asperity deformation during shearing. *International Journal of Rock Mechanics and Mining Sciences* 1997; **34**(1):71–84.
15. Marache A, Hopkins DL, Riss J, Gentier S. Influence of the variation of mechanical parameters on results of the simulation of shear tests on a rock joint. *EUROCK* 2001, Espoo, 3–7 June, 2001; 517–522.
16. Yeo IW, Zimmerman RW, De Freitas MH. The effect of shear displacement on the void geometry of aperture distribution of a rock fracture. *Proceedings of the 3rd Mechanics of Jointed and Faulted Rocks*. Vienna, 6–9 April, 1998; 223–228.
17. Lanaro F. A random field model for surface roughness and aperture of rock fractures. *International Journal of Rock Mechanics and Mining Sciences* 2000; **37**(8):1195–1210.

